nature materials

ARTICLES

https://doi.org/10.1038/s41563-018-0063-z

Highly reversible zinc metal anode for aqueous batteries

Fei Wang[1,2], Oleg Borodin[2], Tao Gao[1], Xiulin Fan[1], Wei Sun[1], Fudong Han[1], Antonio Faraone[3], Joseph A Dura[3], Kang Xu[2*] and Chunsheng Wang[1*]

Metallic zinc (Zn) has been regarded as an ideal anode material for aqueous batteries because of its high theoretical capacity (820 mA h g^{-1}), low potential (−0.762 V versus the standard hydrogen electrode), high abundance, low toxicity and intrinsic safety. However, aqueous Zn chemistry persistently suffers from irreversibility issues, as exemplified by its low coulombic efficiency (CE) and dendrite growth during plating/ stripping, and sustained water consumption. In this work, we demonstrate that an aqueous electrolyte based on Zn and lithium salts at high concentrations is a very effective way to address these issues. This unique electrolyte not only enables dendrite-free Zn plating/stripping at nearly 100% CE, but also retains water in the open atmosphere, which makes hermetic cell configurations optional. These merits bring unprecedented flexibility and reversibility to Zn batteries using either $LiMn_2O_4$ or O_2 cathodes—the former deliver 180 W h kg^{-1} while retaining 80% capacity for > 4,000 cycles, and the latter deliver 300 W h kg^{-1} (1,000 W h kg^{-1} based on the cathode) for >200 cycles.

Since its appearance in the very first battery (Volta Pile, 1799), metallic zinc (Zn) has been regarded as an ideal anode material for aqueous batteries because of its high theoretical capacity (820 mA h g^{-1}), low electrochemical potential (−0.762 V versus (vs) the standard hydrogen electrode (SHE)), high abundance and low toxicity, along with an intrinsic safety from their aqueous nature[1–4]. These advantages directly drove the recent renaissance of rechargeable Zn battery development[5–9]. However, the Zn anode in alkaline electrolytes persistently suffers from severe irreversibility issues caused by the low coulombic efficiency (CE) of its plating/stripping, dendrite growth during cycling, sustained water consumption[10,11] and irreversible by-products, such as Zn hydroxides or zincates. Although Zn dendrite formation could be minimized in neutral electrolytes[1,2], its low plating/stripping CE remains a severe challenge. In most previous reports, high charge/discharge rates had to be used to reduce the effect of poor reversibility on cycling life[5,6,9,12–14], and regularly replenishing the electrolyte with water was often required to compensate the water decomposition[11,15–17]. Zn also had to be used in significant excess to maintain the supply during its consumption by side reactions, which leads to substantial underutilization of its theoretical capacity[18,19].

The expansion in the electrochemical stability window of aqueous electrolytes and other advantages brought about by the recent discovery of water-in-salt electrolytes provide an unprecedented opportunity to resolve the irreversibility issue of a Zn anode in aqueous electrolytes[20–24], which was found to be closely associated with the solvation-sheath structure of the divalent cation[10,25–29]. The strong interaction between Zn^{2+} and water molecules constitutes a high energy barrier for a solvated Zn^{2+} to desolvate and deposit, whereas the generation of a hydroxyl ion (OH^-) via water decomposition often drives the formation of $Zn(OH)_2$, which further converts into insoluble ZnO and becomes electrochemically inactive[11,30]. Strongly bound zincate complexes also promote dendrite formation[1].

Here we report that the highly concentrated Zn-ion electrolyte (denoted as HCZE hereafter) with a supporting salt at a high concentration, 1 m $Zn(TFSI)_2$ + 20 m LiTFSI (where m is molality (mol kg^{-1}); TFSI, bis(trifluoromethanesulfonyl)imide)[24], which is neutral in pH and capable of retaining water in an open atmosphere, promotes dendrite-free plating/stripping of Zn at nearly 100% CE, and brings unprecedented reversibility to aqueous Zn batteries with either $LiMn_2O_4$ or O_2 cathodes. The former delivers 180 W h kg^{-1} and retains 80% of its capacity for >4,000 cycles, whereas the latter delivers 300 W h kg^{-1} for >200 cycles. The structural and spectroscopic studies combined with molecular-scale modelling revealed that this excellent Zn reversibility stems from the unique solvation-sheath structure of Zn^{2+} in the highly concentrated aqueous electrolyte, where the high population of anions forces them into the vicinity of Zn^{2+} to form close ion pairs $(Zn–TFSI)^+$ that significantly suppress the presence of $(Zn–(H_2O)_6)^{2+}$. This fundamental understanding opens up a new avenue to the highly efficient utilization of Zn for advanced energy-storage applications with intrinsic safety, and with potential application for other multivalent cations that are often plagued with poor reversibility and sluggish kinetics.

High Zn reversibility

The reversibility and stability of Zn in HCZE (1 m $Zn(TFSI)_2$ + 20 m LiTFSI) were investigated using a Zn/Zn symmetric cell under galvanostatic condition (Fig. 1a). After >500 cycles (which takes > 170 hours), the Zn plated on the substrates still exhibits a dense and dendrite-free morphology (Fig. 1b), which contains no ZnO according to X-ray diffraction (XRD) (Fig. 1b, inset). In sharp contrast, in an alkaline electrolyte (6 M KOH), a sudden polarization occurs after only six stripping/plating cycles (Supplementary Fig. 1a) due to intensified Zn-dendrite formation, which shorted the cell within 5.3 hours. Consistent with the previous reports, the formation of a ZnO layer was detected by XRD on this cycled Zn surface (Supplementary Fig. 1b)[2]. The reversibility of Zn plating/stripping in HCZE was further investigated using cyclic voltammetry (CV),

[1]Department of Chemical and Biomolecular Engineering, University of Maryland, College Park, MD, USA. [2]Electrochemistry Branch, Sensor and Electron Devices Directorate, Power and Energy Division, US Army Research Laboratory, Adelphi, MD, USA. [3]NIST Center for Neutron Research, National Institute of Standards and Technology, Gaithersburg MD, USA. *e-mail: conrad.k.xu.civ@mail.mil; cswang@umd.edu

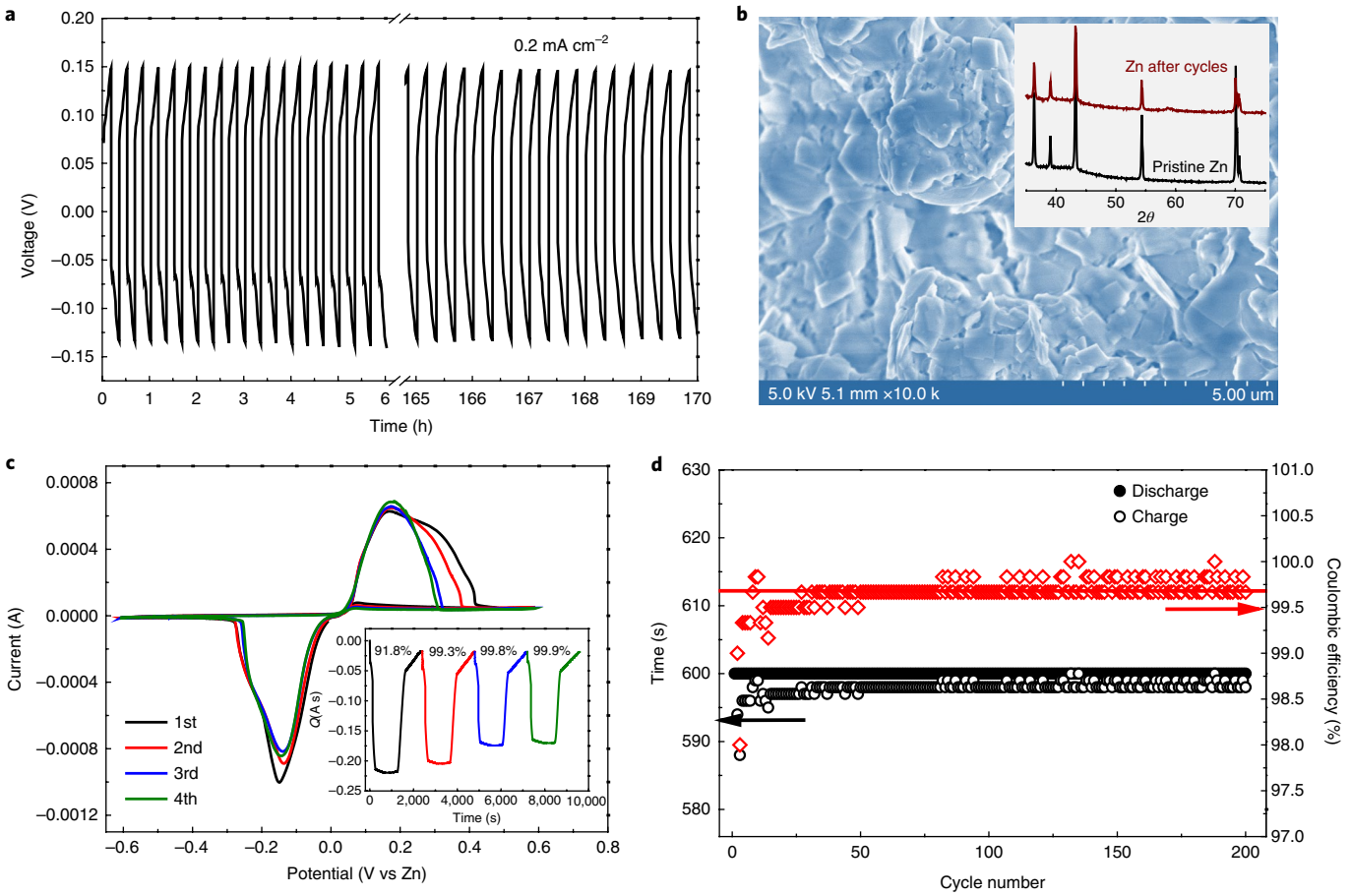

Fig. 1 | Characterization of the Zn anode in HCZE (1 m $Zn(TFSI)_2$ + 20 m LiTFSI). a, Galvanostatic Zn stripping/plating in a Zn/Zn symmetrical cell at 0.2 mA cm^{-2}. **b**, SEM image and XRD pattern (inset) of a Zn anode after 500 stripping/plating cycles in HCZE. **c**, Cyclic voltammogram of Zn plating/stripping in a three-electrode cell using a Pt disc (2 mm in diameter) as the working and Zn as the reference and counter electrodes at a scan rate of 1 mV s^{-1}. Inset: chronocoulometry curves. **d**, The Zn plating/stripping time (left) and CE (right) on a Pt working electrode at 1 mA cm^{-2}.

in which a Pt disk (2 mm in diameter) was used as the working and Zn as the reference and counter electrodes in a three-electrode cell. Chronocoulometry curves (Fig. 1c, inset) reveal that the plating/stripping is highly reversible with the CE approaching 100% after the second cycle, which is similar to that of the ionic liquid-based electrolytes[25,28]. Again, in sharp contrast, the CE in alkaline electrolytes is <50% (Supplementary Fig. 2) under identical conditions. Alternatively, in mildly acidic aqueous electrolytes (2 M $ZnSO_4$ and 2 M $Zn(CH_3COO)_2$), higher CEs of 75% and 80%, respectively, were obtained (Supplementary Fig. 2), but still much inferior when compared to HCZE. Pt/Zn coin cells were also used to evaluate the reversibility of Zn plating/stripping, whose CE, calculated from the ratio of Zn removed from Pt substrate to that deposited during the same cycle, gradually increased and reached 99.5% after the first three cycles (Supplementary Fig. 3). Remarkably, a stable CE of > 99.7% was maintained for >200 cycles, which suggests that essentially all the Zn deposited on the substrate could be recovered during the subsequent stripping process. Interestingly, CEs were found to be highly sensitive to LiTFSI concentrations in HCZE, where they steadily increased from ~80% at 5 m LiTFSI to ~96% at 15 m LiTFSI (Supplementary Fig. 4). Apparently, the high TFSI concentration, which amounts to 22 m (1 m $Zn(TFSI)_2$ + 20 m LiTFSI), could be directly responsible for the high CE of Zn in HCZE.

Solvation-sheath structure of Zn^{2+}

In aqueous solutions, Zn^{2+} cations are solvated by dipolar water molecules, which gives rise to aqua ions $(Zn(OH_2)_6)^{2+}$ as long as there are enough water molecules available. Such cation–solvent interaction has a profound effect on the pH of the resultant solutions because, for the solvated Zn^{2+}, charge transfer occurs via the M–OH_2 bond, with electrons departing the $3a_1$ bonding molecular orbital of the coordinated water for empty Zn^{2+} orbitals, which results in a significantly weakened O–H bond within the water molecule[31,32]. In dilute aqueous solutions, deprotonation would ensue and generate an acidic solution along with a series of more-or-less deprotonated monomeric species, which range from aqua ions $(Zn(OH_2)_6)^{2+}$ to hydroxyl species $Zn(OH)_2$ or even oxo-anions ZnO when all the protons are removed from the coordination sphere of the metal cation[33]. As shown in Fig. 2a, the electrolyte pH values steadily increase with LiTFSI concentration, from pH = 3 at 1.0 m $Zn(TFSI)_2$, where the strong interaction of Zn^{2+} with H_2O leads to hydrolysis[34], all the way to approaching pH ≈ 7 in HCZE, where the near neutrality indicates the effective suppression of hydrolysis. The interplay among Zn^{2+}, $TFSI^-$ and water was quantified using Fourier transform infrared (FTIR) and NMR spectroscopies. A strong band in the FTIR spectra at ~3,552 cm^{-1} (Fig. 2b) together with a small shoulder at ~3,414 cm^{-1} arise for the dilute concentration (1 m $Zn(TFSI)_2$ + 5 m LiTFSI), with the peak at 3,414 cm^{-1} attributed to the weak hydrogen bonding of H_2O, which indicates the aggregation of water molecules[35]. At a salt concentration of 10 m, the 3,414 cm^{-1} peak almost disappears, which indicates the extensive disruption of the water network connected via hydrogen bonding. The ^{17}O chemical shift of the water signal (~0 ppm) in the NMR spectra (Fig. 2c) serves as a sensitive indicator for its coordination with salt ions.

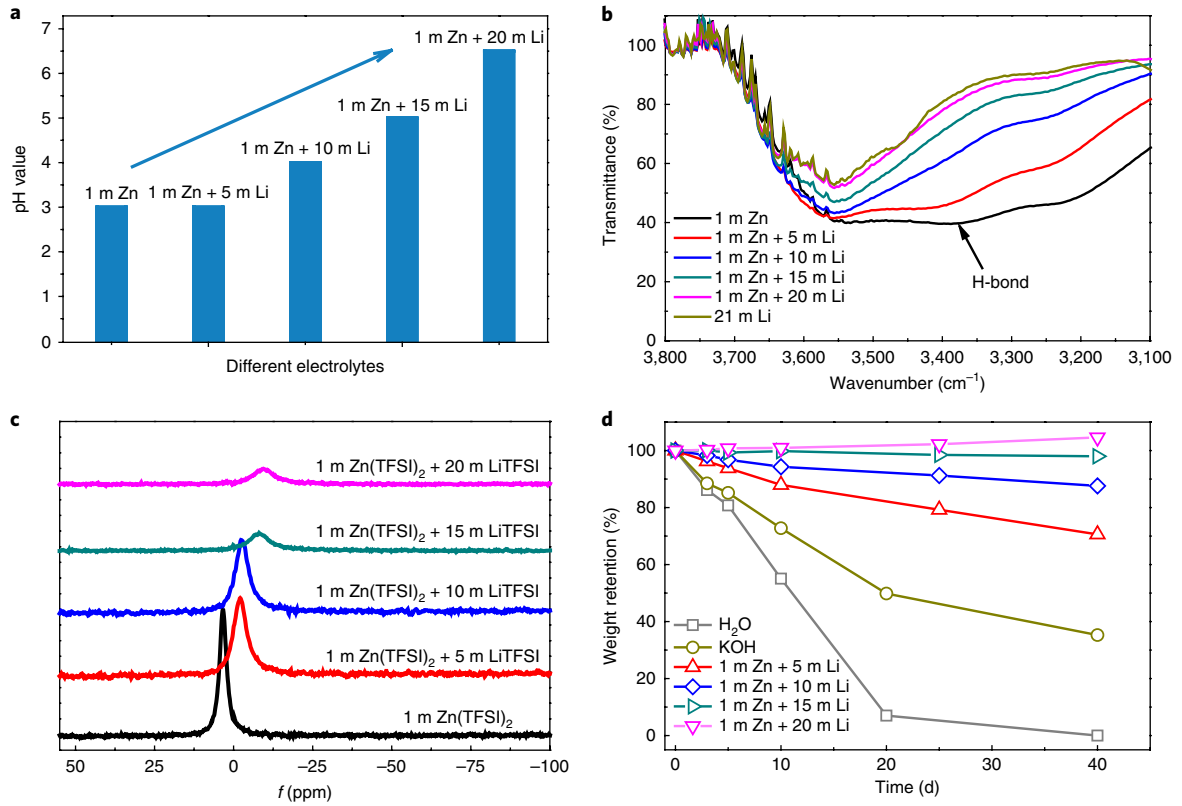

Fig. 2 | The effect of LiTFSI concentration on the cation solvation-sheath structure and bulk properties. a, The pH values of the electrolytes with varying LiTFSI concentrations. **b**, The progression of FTIR spectra with salt concentration between 3,800 and 3,100 cm^{-1}. **c**, The change with salt concentration of chemical shifts for ^{17}O nuclei in solvent (water). **d**, The weight retention of different electrolytes in the air with a relative humidity of ~65%.

With increasing salt concentration, the ^{17}O signal starts a downshift, because the lone-pair electrons on water O are directly depleted by the Li^+ cation, which deshields the O nucleus. This effect apparently intensifies as the salt concentration increases to ~10 m. Based on both the FTIR and ^{17}O-NMR spectra, we believe that, at high Li^+ concentrations, water molecules may have been severely confined within the Li^+ solvation structures, and the presence of water in the vicinity of Zn^{2+} severely diminished. This weakened Zn–water interaction essentially eliminated the hydrolysis effect, as evidenced by the neutral pH value.

Figure 2d demonstrates the weight retention of the electrolytes with varying LiTFSI concentrations when exposed to the open atmosphere. A sharp contrast exists between the dilute (5 m LiTFSI) and the concentrated (10 m LiTFSI and greater) electrolytes. The most concentrated electrolyte (1 m $Zn(TFSI)_2$ + 20 m LiTFSI) not only retains the water content for 40 days, but also experiences a slight weight increase, which indicates that the electrolyte actually extracted moisture from the ambient. This unique feature effectively removes the traditional concern of aqueous Zn electrolytes that regularly require replenishing, and renders the cell with unprecedented flexibility in form factor and durability.

Molecular dynamics (MD) studies

MD simulations were performed using the polarizable APPLE&P force field on aqueous electrolytes that consisted of 1 m $Zn(TFSI)_2$ and LiTFSI at three concentrations (5 m, 10 m and 20 m) as a function of temperature. The force field's ability to describe Zn^{2+} binding to $TFSI^-$ is shown in Supplementary Figs. 5 and 6 and Table 1. Due to the much stronger binding of water and $TFSI^-$ by Zn^{2+} as compared to Li^+, a longer residence time of TFSI in the vicinity of Zn^{2+} was observed as compared to the $Li^+/TFSI^-$ relaxation. Thus, a sequence of MD simulation runs from 450 K (overheated system) to 393 K and 363 K was performed to accelerate the dynamics and to ensure that the equilibrium Zn^{2+}-solvation-sheath structure was obtained (Fig. 3a and Supplementary Fig. 7). Due to the higher thermal fluctuations at these temperatures (393 K and 450 K), Zn^{2+} relaxation is significantly faster, and the resultant Zn^{2+}-solvation-sheath structures adequately converge. In the most dilute electrolyte (1 m $Zn(TFSI)_2$ + 5 m LiTFSI), Zn^{2+} is expected to coordinate with six water molecules without much contribution from the TFSI, as shown in Fig. 3b–d and Supplementary Fig. 7. This finding is in accord with density functional theory (DFT) calculations (Supplementary Fig. 8 and Supplementary Tables 2 and 3) performed on the $Zn(TFSI)_m(H_2O)_n$ clusters immersed in an implicit water solvent, which revealed the preference of Zn^{2+} to coordinate water instead of $TFSI^-$ in dilute solutions. At the intermediate LiTFSI concentration (1 m $Zn(TFSI)_2$ + 10 m LiTFSI (Fig. 3b–d), anions start to occupy the Zn^{2+}-solvation sheath, which results in a temperature-dependent composition of the Zn^{2+}-solvation shell. In other words, for the electrolytes of intermediate concentrations, increasing temperatures favour the formation of cation–anion aggregates that could be beneficial for anion reduction rather than water. In the most concentrated electrolyte (1 m $Zn(TFSI)_2$ + 20 m LiTFSI), the Zn^{2+}-solvation sheath is occupied primarily by TFSI, with six coordinating oxygens all from TFSI (Fig. 3b–d and Supplementary Fig. 7). Small-angle neutron scattering (SANS) measurements were performed to validate the intermediate-range electrolyte structures predicted by MD simulations, which confirmed the position and shape of an $I(Q)$ peak at $Q \approx 0.5\ A^{-1}$ (Fig. 3e), which originates largely from the D_2O–D_2O correlations with a minor contribution from the ion–ion interaction[36].

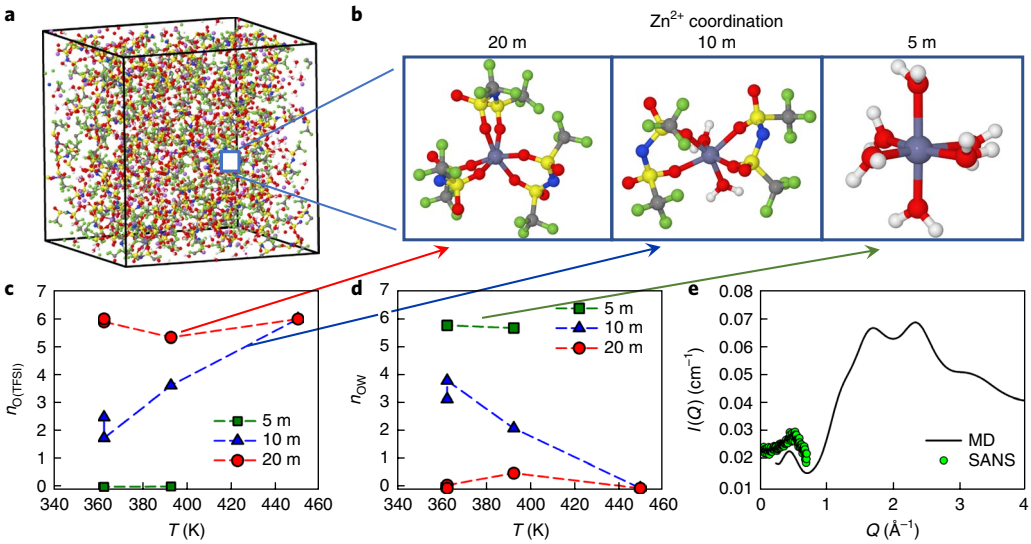

Fig. 3 | MD studies of the Zn^{2+}-solvation structure. a, Snapshot of the MD simulation cell for HCZE (1 m $Zn(TFSI)_2$ + 20 m LiTFSI) at 363 K. **b**, Representative Zn^{2+}-solvation structures in the electrolytes with 1 m $Zn(TFSI)_2$ and three concentrations of LiTFSI (5 m, 10 m and 20 m). **c**,**d**, Zn^{2+}–O(TFSI) (**c**) and Zn^{2+}–O(water) (**d**) coordination numbers for aqueous electrolytes with 1 m $Zn(TFSI)_2$ and three concentrations of LiTFSI (5 m, 10 m and 20 m). **e**, The experimental SANS curve (green circles) and the simulated form (black line) at 298 K for 1 m $Zn(TFSI)_2$ + 20 m LiTFSI electrolyte in D_2O.

DFT calculations also predicted that $Zn(TFSI)_2(H_2O)_2$ clusters found in the 1 m $Zn(TFSI)_2$ + 10 m LiTFSI electrolyte undergo reduction at around 2.55 V vs Li/Li^+, which results in H_2 evolution (Supplementary Fig. 9). TFSI reduction in such clusters would occur at lower potentials (1.6~2.1 V vs Li/Li^+), which indicates that H_2 evolution is expected to be the predominant reaction as long as water molecules are present in the Zn^{2+}-solvation sheath. In the concentrated electrolyte (1 m $Zn(TFSI)_2$ + 20 m LiTFSI), however, water is no longer present in the Zn^{2+}-solvation sheath, and consequently the reduction potential of the $Zn(TFSI)_n$ solvate is increased. Note that the defluorination reaction of LiTFSI occurs at a potential above that of H_2 evolution at high TFSI concentrations[23]. This crossover is critically meaningful for the formation of an effective interphase, whose presence prevents hydrogen evolution at a lower potential and enables an almost quantitative plating/stripping chemistry (CE ≈ 100%) of Zn.

Aqueous Zn/$LiMn_2O_4$ hybrid battery

To demonstrate the reversibility of the Zn anode in an actual full battery, $LiMn_2O_4$ was used as the cathode to couple with Zn in HCZE and form a hybrid battery in which the well-established Li^+ intercalation–deintercalation happens at $LiMn_2O_4$ in a highly reversible manner, whereas Zn strips/plates at the Zn anode. Thus, the CE of Zn stripping/plating dictates the overall electrochemical reversibility of this hybrid chemistry. Unlike the frequent practice of Zn batteries, wherein excessive Zn metal has to be used to prevent premature depletion, the mass ratio between Zn and $LiMn_2O_4$ was set to 0.8:1 in this work to leverage the high Zn stripping/plating CE. Figure 4a shows the charge/discharge profiles of this hybrid battery at a 0.2 C rate, consistent with the typical $LiMn_2O_4$ charge/discharge profiles. The capacity calculated based on the (cathode + anode) mass is 66 mA h g^{-1}, which corresponds to an energy density of 119 W h kg^{-1}. By further reducing the Zn:$LiMn_2O_4$ mass ratio to 0.25:1, a higher energy density of 180 W h kg^{-1} was achieved (Supplementary Fig. 10).

The Zn/$LiMn_2O_4$ full-cell functions with both a high cycling stability and a high columbic efficiency at low (0.2 C) and high (4 C) rates (Fig. 4b,c). At 0.2 C, an excellent stability with a high capacity retention of 83.8% and a CE of 99.9% for 500 cycles was observed; at 4 C, 85% of the initial capacity could still be retained after 4,000 cycles, with a high CE of 99.9%. The effect of LiTFSI concentration on the electrochemical performance of Zn/$LiMn_2O_4$ cells was also investigated (Supplementary Fig. 11). The mass ratio of Zn:$LiMn_2O_4$ was again set at 0.8:1. For the intermediate LiTFSI concentration (1 m $Zn(TFSI)_2$ + 15 m LiTFSI), the capacity retention after 100 cycles was 75%, along with an average CE of ~99%, whereas at the lower LiTFSI concentration (1 m $Zn(TFSI)_2$ + 10 m LiTFSI) the capacity retention dropped to 59.5% after 100 cycles with the average CE of ~97%. In sharp contrast, the cell using the dilute electrolyte (1 m $Zn(TFSI)_2$ + 5 m LiTFSI) showed a rather low CE of ~90% during the first 20 cycles, and the capacity rapidly decayed to zero after only 25 cycles. The low CE, rather than Zn-dendrite formation, is considered responsible for the limited cycle number in this case, as no short circuit was observed. Theoretically, a nearly 100% CE is required to achieve the long-term cycling stability of zinc batteries[37,38], otherwise excessive Zn metal has to be used to compensate for the incessant Zn consumption, which drives down the actual specific-capacity utilization and energy density. The parasitic reactions in Zn/$LiMn_2O_4$ were evaluated by monitoring the open-circuit-voltage decay of a fully charged cell during storage and then discharging after 24 hours of storage. 97.8% of the original capacity was retained (Fig. 4d), which confirms that the parasitic H_2 and O_2 evolutions during storage remain negligible.

Finally, we attempted to estimate the full-cell energy density on a more practical basis by also including the electrolyte weight. It was found that because the above 'Zn–Li' hybrid battery is at a discharged state upon assembly, its energy density relies on how much Zn^{2+} is prestored in the pristine electrolyte, which is limited by the Zn salt solubility. Thus, the full-cell energy density decreases to an unsatisfactory level if all the Zn has to be present in the pristine electrolytes. To mitigate this disadvantage, we circumvented the above limitation by assembling the cell in its charged state, that is, coupling a MnO_2 cathode with a Zn anode. In this configuration, Zn is stored at the anode, whereas an electrolyte with a low Zn salt concentration (0.2 m $Zn(TFSI)_2$ + 21 m LiTFSI) was used. When such a Zn/MnO_2 cell experiences the initial discharge, Zn^{2+} dissolves from the anode and gradually displaces Li^+ in the electrolyte, whereas Li^+ leaves the electrolyte and intercalates into the MnO_2

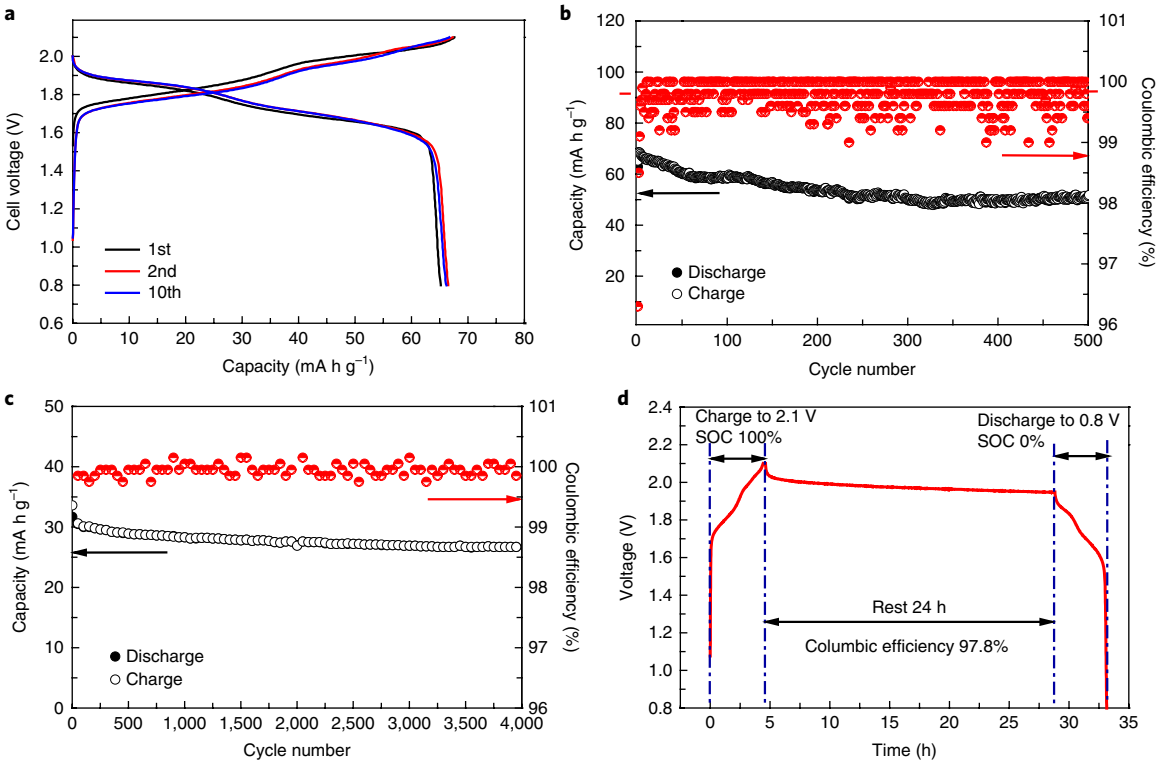

Fig. 4 | Electrochemical performance of the Zn/$LiMn_2O_4$ full cell. a, A typical voltage profile of the Zn/$LiMn_2O_4$ full cell in HCZE (1 m $Zn(TFSI)_2$ + 20 m LiTFSI) at a constant current (0.2 C; areal capacity of $LiMn_2O_4$, 2.4 mA h cm^{-2}). **b**,**c**, The cycling stability and CE of the Zn/$LiMn_2O_4$ full cell in HCZE at 0.2 C (**b**) and 4 C (**c**) rates. **d**, Storage performance evaluated by resting for 24 h at 100% state of charge (SOC) after ten cycles at 0.2 C, followed by full discharging.

lattice. Benefitting from the high CE of both Zn stripping/plating and Li^+ intercalation/de-intercalation, the overall cell reversibility is almost identical to that of the discharged full-cell Zn/$LiMn_2O_4$ (Supplementary Fig. 12), but the energy density could now reach a high level of 70 W h kg^{-1} based on the total weight of the anode, cathode and electrolyte.

Highly reversible aqueous Zn/O_2 battery

To demonstrate the versatility of HCZE, a Zn/O_2 battery was assembled using Zn as the anode and a porous carbon substrate as the air cathode. Such a chemistry promises an attractive theoretical energy density and has been considered a preferable candidate for large-scale energy-storage applications. Although primary Zn–air batteries have been well developed, their rechargeability has always been hindered by poor Zn reversibility as well as by inefficient air cathodes, in which the cell reactions must occur at triphase sites. Previous efforts at rechargeable Zn/O_2 systems mainly focused on developing bifunctional catalysts for the air cathode[16,39–43], with limited attention given to electrolytes[44,45]. Commonly used alkaline electrolytes are known to induce poor Zn reversibility and cause significant passivation on the air cathode, mainly due to the presence of atmospheric CO_2. However, the neutral pH of HCZE simultaneously stabilizes Zn and the air cathode. Thus, a Zn/O_2 cell with a porous air cathode constructed on carbon paper was examined in the full range between 0.5 and 2.0 V at 50 mA g^{-1}. Here the specific capacity and the current density are based on the active materials of O_2 electrodes because the carbon paper is inactive (Supplementary Fig. 13). Such a cell delivers a highly reversible capacity of nearly 3,000 mA h g^{-1} at an average discharge potential of 0.9 V (Fig. 5a), which, along with the 1.9 V charge potential, is superior to most Zn–air batteries reported in alkaline electrolytes. Unlike alkaline electrolytes, in which the formation of zincate ions ($Zn(OH)_4^{2-}$) prevails, instead ZnO was formed after the first discharge process, as confirmed by the Raman spectrum (Supplementary Fig. 14). The cell voltage fluctuates when the cell is deep discharged, which is believed to be induced by resistance hiking and the subsequent change in the oxygen reduction reaction kinetics. This could be caused by the overproduction of an insulating species, ZnO, on the porous air cathode. To clarify whether Li^+ or Zn^{2+} participates in the reaction with the air cathode, a blank experiment was conducted using excess $LiFePO_4$ to couple with the same air electrode in a Zn-ion-free electrolyte (21 m LiTFSI electrolyte). This cell showed a much lower capacity, lower CE, higher overpotential and extremely slow kinetics (Supplementary Fig. 15). Thus, we conclude that the Zn^{2+} reaction with O_2 at the air cathode dominates the cell chemistry with a reaction mechanism actually similar to that of Li/O_2 or other metal–air chemistries that employ either non-aqueous or ionic liquid electrolytes[44,46]. Given that no catalyst was used in the above Zn/O_2 cell, further improvements in the round-trip energy efficiency are very likely if proper bifunctional catalysts or redox mediators are adopted.

The capacity of the Zn/O_2 cell remained stable for ten cycles and then slowly decayed to 1,000 mA h g^{-1} in 40 cycles, which should be caused by the degradation of the O_2 cathode (Supplementary Fig. 16). The cell was also cycled under a constant-capacity mode of 1,000 mA h g^{-1} (Fig. 5b), which corresponds to a full-cell energy density of 300 W h kg^{-1} (based on the cathode and anode, or 160 W h kg^{-1} with the electrolyte weight included). Limiting the capacity utilization allows the cycle life to be extended beyond 200 cycles, with the polarization slightly increasing with cycle number. Apparently, the concentrated and neutral HCZE, with its unique water-retaining capability, enables a Zn/O_2 cell with an excellent cycle life, high efficiency and good capacity utilization not observed in any conventional Zn aqueous electrolytes known thus far.

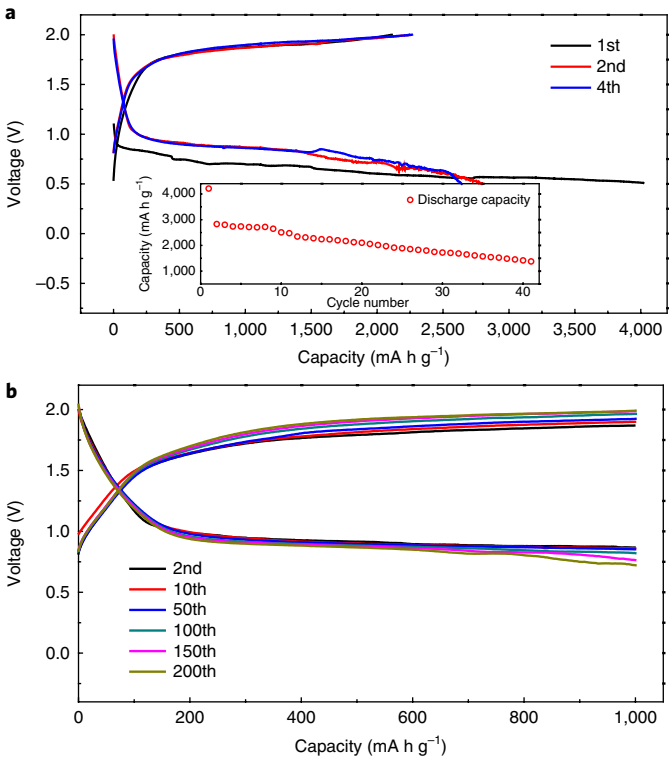

Fig. 5 | Electrochemical performance of the aqueous Zn/O_2 full cell. a, Typical full-range voltage profile of the Zn/O_2 battery in HCZE (1 m $Zn(TFSI)_2$ + 20 m LiTFSI) using 70 wt% super P as the air cathode at a constant current of 50 mA g^{-1} (based on the cathode) between 0.5 and 2.0 V. Inset: corresponding cycling performance. **b**, Cycling performance of the Zn/O_2 battery at a current density of 50 mA g^{-1} under a constant capacity mode (1,000 mA h g^{-1}; the areal capacity of the cathode was 0.7 mA h cm^{-2}).

Conclusions

The highly concentrated aqueous electrolyte (1 m $Zn(TFSI)_2$ + 20 m LiTFSI) enables a wide variety of unique properties that are otherwise unavailable from dilute Zn electrolytes. The MD simulations and structural and spectroscopic studies establish a direct correlation between the Zn^{2+}-solvation-sheath structure and Zn anode reversibility. At LiTFSI concentrations ≥20 m, in which Zn^{2+} is surrounded by $TFSI^-$ instead of water, H_2 evolution is effectively prevented, which leads to a reversible and dendrite-free Zn plating/stripping (CE ≈ 100%). Leveraging this high reversibility, a few Zn batteries were demonstrated, all of which outperform their counterparts in dilute aqueous Zn electrolytes. The hybrid Zn–Li battery (Zn/$LiMn_2O_4$) delivers an excellent cycle performance, with an 85% capacity retained after 4,000 cycles at a CE of 99.9%. The more challenging Zn/O_2 system delivers an unprecedented high energy density of 300 W h kg^{-1} for 200 cycles. In particular, the neutral pH and excellent water-retention capability of this new Zn aqueous electrolyte significantly benefits the application of a Zn/air battery, which has been plagued by the alkaline nature of the electrolytes and their tendency to lose water via both parasitic reactions and evaporation. The intrinsic safety and excellent cyclability makes these Zn batteries potential candidates for the application in some extreme conditions, such as in aerospace, airplanes, submarines, deep-ocean survey vehicles and other military applications. Inspired by this concept, an alternative electrolyte (0.5 m zinc trifluoromethanesulfonate ($Zn(OTf)_2$) + 18 m $NaClO_4$) provides an excellent CE of ~98% at a much lower cost (Supplementary Fig. 17). The fundamental understanding and the above demonstrations of successful batteries open a viable route to the development of Zn batteries with high energy, high reversibility and high safety, which could also be extended to other multivalent cations.

Methods

Methods, including statements of data availability and any associated accession codes and references, are available at https://doi.org/10.1038/s41563-018-0063-z.

Received: 12 June 2017; Accepted: 20 March 2018;
Published online: 16 April 2018

References

1. Kundu, D., Adams, B. D., Duffort, V., Vajargah, S. H. & Nazar, L. F. A high-capacity and long-life aqueous rechargeable zinc battery using a metal oxide intercalation cathode. *Nat. Energy* **1**, 16119 (2016).
2. Pan, H. et al. Reversible aqueous zinc/manganese oxide energy storage from conversion reactions. *Nat. Energy* **1**, 16039 (2016).
3. Parker, J. F. et al. Rechargeable nickel–3D zinc batteries: an energy-dense, safer alternative to lithium-ion. *Science* **356**, 415–418 (2017).
4. Luo, J. Y., Cui, W. J., He, P. & Xia, Y. Y. Raising the cycling stability of aqueous lithium-ion batteries by eliminating oxygen in the electrolyte. *Nat. Chem.* **2**, 760–765 (2010).
5. Yesibolati, N. et al. High performance Zn/$LiFePO_4$ aqueous rechargeable battery for large scale applications. *Electrochim. Acta.* **152**, 505–511 (2015).
6. Wu, X. et al. The electrochemical performance improvement of $LiMn_2O_4$/Zn based on zinc foil as the current collector and thiourea as an electrolyte additive. *J. Power Sources* **300**, 453–459 (2015).
7. Trocoli, R. & La Mantia, F. An aqueous zinc-ion battery based on copper hexacyanoferrate. *ChemSusChem.* **8**, 481–485 (2015).
8. Wang, X. et al. An aqueous rechargeable Zn//Co_3O_4 battery with high energy density and good cycling behavior. *Adv. Mater.* **28**, 4904–4911 (2016).
9. Zhang, L., Chen, L., Zhou, X. & Liu, Z. Towards high-voltage aqueous metal-ion batteries beyond 1.5 V: the zinc/zinc hexacyanoferrate system. *Adv. Energy Mater.* **5**, 1400930 (2015).
10. Liu, Z. et al. Dendrite-free nanocrystalline zinc electrodeposition from an ionic liquid containing nickel triflate for rechargeable Zn-based batteries. *Angew. Chem. Int. Ed.* **55**, 2889–2893 (2016).
11. Li, Y. & Dai, H. Recent advances in zinc–air batteries. *Chem. Soc. Rev.* **43**, 5257–5275 (2014).
12. Li, G., Yang, Z., Jiang, Y., Zhang, W. & Huang, Y. Hybrid aqueous battery based on $Na_3V_2(PO_4)_3$/C cathode and zinc anode for potential large-scale energy storage. *J. Power Sources* **308**, 52–57 (2016).
13. Zhang, H., Du, Q., Li, C. & Sun, X. Binary ion batteries operating on the model of Newton's cradle. *J. Electrochem. Soc.* **159**, A2001–A2004 (2012).
14. Yan, J. et al. Rechargeable hybrid aqueous batteries. *J. Power Sources* **216**, 222–226 (2012).
15. Xu, M., Ivey, D. G., Xie, Z. & Qu, W. Rechargeable Zn–air batteries: progress in electrolyte development and cell configuration advancement. *J. Power Sources* **283**, 358–371 (2015).
16. Fu, J. et al. Flexible high-energy polymer-electrolyte-based rechargeable zinc–air batteries. *Adv. Mater.* **27**, 5617–5622 (2015).
17. Pei, P., Wang, K. & Ma, Z. Technologies for extending zinc–air battery's cyclelife: a review. *Appl. Energy* **128**, 315–324 (2014).
18. Qian, J. et al. High rate and stable cycling of lithium metal anode. *Nat. Commun.* **6**, 6362 (2015).
19. Xu, W. et al. Lithium metal anodes for rechargeable batteries. *Energy Environ. Sci.* **7**, 513–537 (2014).
20. Parker, J. F. et al. Retaining the 3D framework of zinc sponge anodes upon deep discharge in Zn–air cells. *ACS Appl. Mater. Interfaces* **6**, 19471–19476 (2014).
21. Parker, J. F., Chervin, C. N., Nelson, E. S., Rolison, D. R. & Long, J. W. Wiring zinc in three dimensions re-writes battery performance—dendrite-free cycling. *Energy Environ. Sci.* **7**, 1117 (2014).
22. Chamoun, M. et al. Hyper-dendritic nanoporous zinc foam anodes. *NPG Asia Mater.* **7**, e178 (2015).
23. Banik, S. J. & Akolkar, R. Suppressing dendrite growth during zinc electrodeposition by PEG-200 additive. *J. Electrochem. Soc.* **160**, D519–D523 (2013).
24. Suo, L. et al. 'Water-in-salt' electrolyte enables high-voltage aqueous lithium-ion chemistries. *Science* **350**, 938–943 (2015).
25. Guerfi, A. et al. High cycling stability of zinc-anode/conducting polymer rechargeable battery with non-aqueous electrolyte. *J. Power Sources* **248**, 1099–1104 (2014).
26. Xu, M., Ivey, D. G., Xie, Z., Qu, W. & Dy, E. The state of water in 1-butyl-1-methyl-pyrrolidinium bis(trifluoromethanesulfonyl)imide and its effect on Zn/Zn(ii) redox behavior. *Electrochim. Acta.* **97**, 289–295 (2013).

27. Xu, M., Ivey, D. G., Xie, Z. & Qu, W. Electrochemical behavior of Zn/Zn(ii) couples in aprotic ionic liquids based on pyrrolidinium and imidazolium cations and bis(trifluoromethanesulfonyl)imide and dicyanamide anions. *Electrochim. Acta.* **89**, 756–762 (2013).
28. Xu, M. et al. Zn/Zn(ii) redox kinetics and Zn deposit morphology in water added ionic liquids with bis(trifluoromethanesulfonyl)imide anions. *J. Electrochem. Soc.* **161**, A128–A136 (2013).
29. Han, S. D. et al. Origin of electrochemical, structural, and transport properties in nonaqueous zinc electrolytes. *ACS Appl. Mater. Interfaces* **8**, 3021–3031 (2016).
30. Liu, Z., El Abedin, S. Z. & Endres, F. Dissolution of zinc oxide in a protic ionic liquid with the 1-methylimidazolium cation and electrodeposition of zinc from ZnO/ionic liquid and ZnO/ionic liquid–water mixtures. *Electrochem. Commun.* **58**, 46–50 (2015).
31. Barnum, D. W. Hydrolysis of cations. Formation constants and standard free energies of formation of hydroxy complexes. *Inorg. Chem.* **22**, 2297–2305 (1983).
32. Sze, Y.-K. & Irish, D. E. Vibrational spectral studies of ion–ion and ion–solvent interactions. I. Zinc nitrate in water. *J. Solut. Chem.* **7**, 395–415 (1978).
33. Smith, G. D., Bell, R., Borodin, O. & Jaffe, R. L. A density functional theory study of the structure and energetics of zincate complexes. *J. Phys. Chem. A* **105**, 6506–6512 (2001).
34. Barnum, D. W. Hydrolysis of cations—formation-constants and standard free-energies of formation of hydroxy complexes. *Inorg. Chem.* **22**, 2297–2305 (1983).
35. Scatena, L., Brown, M. & Richmond, G. Water at hydrophobic surfaces: weak hydrogen bonding and strong orientation effects. *Science* **292**, 908–912 (2001).
36. Borodin, O. et al. Liquid structure with nano-heterogeneity promotes cationic transport in concentrated electrolytes. *ACS Nano* **11**, 10462–10471 (2017).
37. Smith, A., Burns, J. & Dahn, J. A high precision study of the Coulombic efficiency of Li-ion batteries. *Electrochem. Solid State Lett.* **13**, A177–A179 (2010).
38. Burns, J. et al. Predicting and extending the lifetime of Li-ion batteries. *J. Electrochem. Soc.* **160**, A1451–A1456 (2013).
39. Zhang, J. et al. Laminated cross-linked nanocellulose/graphene oxide electrolyte for flexible rechargeable zinc–air batteries. *Adv. Energy Mater.* **6**, 1600476 (2016).
40. Xu, N. et al. Self-assembly formation of bi-functional Co_3O_4/MnO_2–CNTs hybrid catalysts for achieving both high energy/power density and cyclic ability of rechargeable zinc–air battery. *Sci. Rep.* **6**, 33590 (2016).
41. Suren, S. & Kheawhom, S. Development of a high energy density flexible zinc–air battery. *J. Electrochem. Soc.* **163**, A846–A850 (2016).
42. Liu, X. et al. High-performance non-spinel cobalt–manganese mixed oxide-based bifunctional electrocatalysts for rechargeable zinc–air batteries. *Nano Energy* **20**, 315–325 (2016).
43. Li, G. et al. Pomegranate-inspired design of highly active and durable bifunctional electrocatalysts for rechargeable metal–air batteries. *Angew. Chem. Int. Ed.* **55**, 4977–4982 (2016).
44. Kar, M., Simons, T. J., Forsyth, M. & MacFarlane, D. R. Ionic liquid electrolytes as a platform for rechargeable metal–air batteries: a perspective. *Phys. Chem. Chem. Phys.* **16**, 18658–18674 (2014).
45. Ho, C. C., Evans, J. W. & Wright, P. K. Direct write dispenser printing of a zinc microbattery with an ionic liquid gel electrolyte. *J. Micromech. Microeng.* **20**, 104009 (2010).
46. Lu, J. et al. A lithium–oxygen battery based on lithium superoxide. *Nature* **529**, 377–382 (2016).

Acknowledgements

The principal investigators (K.X. and C.W.) gratefully acknowledge funding support from DOE ARPA-E (DEAR0000389) and the Center of Research on Extreme Batteries. We also acknowledge the support of the Maryland Nano Center and its NispLab. NispLab is supported in part by the NSF as a MRSEC Shared Experimental Facility. O.B. acknowledges Army funding DRI16-SE-019 for modelling. F.W. was supported by the Oak Ridge Associated Universities through contract W911NF-16-2-0202.

Author contributions

F.W., K.X. and C.W. conceived the idea and co-wrote the manuscript. O.B. conducted the MD simulations and DFT calculations. A.F. and J.A.D. conducted the SANS measurements. F.W. carried out the synthesis, material characterizations, and electrochemical evaluation. T.G., X.F., W.S. and F.H. assisted with the material characterizations.

Additional information

Supplementary information is available for this paper at https://doi.org/10.1038/s41563-018-0063-z.

Reprints and permissions information is available at www.nature.com/reprints.

Correspondence and requests for materials should be addressed to K.X. or C.W.

Publisher's note: Springer Nature remains neutral with regard to jurisdictional claims in published maps and institutional affiliations.

Methods

Materials. $LiN(SO_2CF_3)_2$ (LiTFSI), $Zn(N(SO_2CF_3)_2)_2$ ($Zn(TFSI)_2$) and $Zn(CF_3SO_3)_2$ were purchased from Tokyo Chemical Industry. The electrolyte (20 m LiTFSI + 1 m $Zn(TFSI)_2$) was prepared by dissolving LiTFSI and $Zn(TFSI)_2$ in water according to the molality (20 mol LiTFSI and 1 mol $Zn(TFSI)_2$ in 1 kg water). Zinc foil (0.1 mm thick) was purchased from Alfa Aesar. Zinc powder (40–60 nm) and $NaClO_4$ were purchased from Sigma-Aldrich. Polyvinylidene fluoride (PVDF) and $LiMn_2O_4$ were purchased from MTI Corporation. Carbon paper was purchased from FuelCellStore. (Certain commercial equipment, instruments and materials are identified in this paper to foster understanding. Such identification does not imply recommendation or endorsement by the National Institute of Standards and Technology (NIST), nor does it imply that the materials or equipment mentioned are necessarily the best available for the purpose).

Materials characterizations. The morphology of the sample was investigated by scanning electron microscopy (SEM, Hitachi SU-70). All the samples for ex situ SEM were recovered from a full aqueous battery in a 2032 coin-cell configuration after electrochemical cycling. XRD patterns were obtained on a Bruker Smart 1000 (Bruker AXS, Inc.) using Cu Kα radiation with an airtight holder from Bruker. FTIR was performed with a Nicolet 6700 spectrometer instrument and a Golden Gate single-reflection monolithic diamond attenuated total reflection sample cell. The ^{17}O NMR experiments were done with a 400 SB Bruker Avance III spectrometer, using 5 mm tubes.

Electrochemical measurements. The zinc anode was prepared by mixing 80% zinc powder, 10% carbon black and 10% PVDF in *N*-methylpyrrolidinone (NMP) and the slurry mixture was then coated on Al foil. The $LiMn_2O_4$ cathode was prepared by compressing active material, carbon black and polytetrafluoroethylene (PTFE) at weight ratio of 8:1:1 onto the stainless steel mesh. The O_2 cathode was prepared by mixing 70% carbon black and 30% PVDF in NMP and the slurry mixture was then coated on carbon paper. After coating, the electrodes were dried at 80 °C for 10 min to remove the solvent before pressing. The electrodes were cut into 1 cm^2 sheets, vacuum dried at 100 °C for 24 h and weighed before assembly. CV was carried out using a CHI 600E electrochemical work station. The charge–discharge experiments were performed on a Land BT2000 battery test system (Wuhan) at room temperature.

SANS measurements. SANS measurements were performed at the NIST Center for Neutron Research at NIST on the 30 m SANS instrument located on neutron guide 7 (ref. [47]). Samples were contained in standard titanium demountable cells with quartz windows and a 1 mm path length. During the experiment the samples were kept at 30 °C using a thermal bath, which allows for a temperature control better than ±0.1°C. The incoming neutron wavelength λ was 5 Å with a $\Delta\lambda/\lambda = 14\%$. The raw scattering data were corrected for background, empty cell and sample transmission to obtain one-dimensional scattering patterns as a function of the exchanged wavevector $Q = 4\pi/\lambda\sin(\theta/2)$ (θ being the scattering angle)[48]. Throughout this manuscript uncertainties and error bars represent one standard error.

DFT study of Zn coordination. The Zn^{2+} cation competitive solvation by water and $TFSI^-$ anions was investigated using DFT. Calculations were performed on the $Zn(TFSI)_m$ and $Zn(H_2O)_n$ clusters in the gas phase and in an implicit solvent using the solvation model based on density (SMD) developed by the Truhlar group[49]. The built-in SMD parameters for water in g09 Gaussian software were used with $\varepsilon = 78.3553$ (ref. [49]). Gaussian 09 (revision c) software was used for all the quantum chemistry calculations. A pruned (99,590) ultrafine integration grid was used, which corresponded to the int = UltraFine keyword. Based on the previous benchmark calculations of the Zn-coordinated complexes, the M05-2×DFT functional was chosen because it was demonstrated to yield accurate geometric parameters, dipole moments and bond-dissociation energies for Zn centres[50].

MD studies. MD simulations were performed on aqueous electrolytes doped with 1 m $Zn(TFSI)_2$ and three concentrations of LiTFSI salts, 5 m, 10 m and 20 m, as a function of temperature. The simulation cell contained nine $Zn(TFSI)_2$, 92 LiTFSI and 1,024 water for the 5 m LiTFSI + 1 m $Zn(TFSI)_2$ electrolyte, 18 $Zn(TFSI)_2$, 184 LiTFSI and 1,024 water for the 10 m LiTFSI + 1 m $Zn(TFSI)_2$ electrolyte and nine $Zn(TFSI)_2$, 174 LiTFSI and 484 water for the 20 m LiTFSI + 1 m $Zn(TFSI)_2$ electrolyte. The previously developed many-body polarizable force field (APPLE&P) was used for the LiTFSI and H_2O terms[24].

The Ewald summation method was used in MD simulations for the electrostatic interactions between permanent charges with permanent charges and permanent charges with induced dipole moments with $k = 7^3$ vectors. Multiple timestep integration was employed with an inner timestep of 0.5 fs (bonded interactions), a central time step of 1.5 fs for all non-bonded interactions within a truncation distance of 7.0–8.0 Å and an outer timestep of 3.0 fs for all non-bonded interactions between 7.0 Å and the non-bonded truncation distance of of 19 Å. The reciprocal part of Ewald was updated only at the largest of the multiple timesteps. A Nose–Hoover thermostat and a barostat were used to control the temperature and pressure with the associated frequencies of 10^{-2} and 0.1×10^{-4} fs. The stress tensor was saved every 9 fs to calculate stress, the tensor autocorrelation function and viscosity, and the atomic coordinates were saved every 2 ps for post-analysis.

Data availability. Experimental data are available from the corresponding author upon reasonable request.

References

47. Glinka, C. et al. The 30 m small-angle neutron scattering instruments at the National Institute of Standards and Technology. *J. Appl. Crystallogr.* **31**, 430–445 (1998).
48. Kline, S. R. Reduction and analysis of SANS and USANS data using IGOR Pro. *J. Appl. Crystallogr.* **39**, 895–900 (2006).
49. Marenich, A. V., Cramer, C. J. & Truhlar, D. G. Universal solvation model based on solute electron density and on a continuum model of the solvent defined by the bulk dielectric constant and atomic surface tensions. *J. Phys. Chem. B* **113**, 6378–6396 (2009).
50. Amin, E. A. & Truhlar, D. G. Zn coordination chemistry: development of benchmark suites for geometries, dipole moments, and bond dissociation energies and their use to test and validate density functionals and molecular orbital theory. *J. Chem. Theor. Comput.* **4**, 75–85 (2008).